# Fourier-Bessel Field Calculation and Tuning of a CW Annular Array

Paul D. Fox, Jiqi Cheng, and Jian-yu Lu, *Senior Member, IEEE*

***Abstract*—A 1-D Fourier-Bessel series method for computing and tuning the linear lossless field of flat continuous wave (CW) annular arrays is given and discussed with both numerical simulation and experimental verification. The technique provides a new method for modelling and manipulating the propagated field by linking the quantized surface pressure profile to a set of limited diffraction Bessel beams propagating into the medium. In the limit, these become a known set of nondiffracting Bessel beams satisfying the lossless linear wave equation, which allow us to derive a linear matrix formulation for the field in terms of the ring pressures on the transducer surface. Tuning (beamforming) of the field then follows by formulating a least squares design with respect to the transducer ring pressures. Results are presented in the context of a 10-ring annular array operating at 2.5 MHz in water.**

## I. Introduction

In this paper, we describe a method for computing and tuning linear lossless fields from flat CW annular arrays using 1-D Fourier-Bessel series [1], [2]. The use of these series allows the propagated field to be described as a set of $J_0$ Bessel beams [3], [4], giving a linear mapping between the spatial ring pressures on the transducer surface and the propagated field at any point in space. Bessel beams have already been extensively studied [5]–[8], and this work builds on previous knowledge to draw up a method for both computing and tuning (beamforming) the propagated field by using a set of Bessel beam basis functions. In [9], these were applied across the transducer surface to decompose the emitted field into a known set of limited diffraction Bessel beams. In this paper, we extend the analysis to include the entire plane beyond the outer edge of the transducer, which, in the limit, describes the emitted field as a set of known nondiffracting Bessel beams. This feature allows us to apply analytic techniques to solve for the field as a weighted set of exact Bessel solutions to the wave equation, constituting a new field analysis tool complimenting other approaches such as [10]–[14]. We show that the method correlates well with both previous experimental results [5] and simulations based on the (slower) Rayleigh-Sommerfeld diffraction formula. The method also allows us to tune the field in a least squares sense with respect to a given desired field distribution. This has been introduced briefly through simulations in [15], modelling the tuning of a Bessel beam on an equal area annular array. In this paper, we extend the method to different tuning designs and an alternative array geometry [5].

Section II gives model definitions for the governing wave equation and structure of the CW annular arrays considered. Section III introduces the application and interpretation of 1-D Fourier-Bessel series in the context of annular arrays. In Section IV, we explain how to compute the propagated field using Fourier-Bessel series, with a numerical example provided in Section V. Section VI then extends the analysis of the field propagation to derive a least squares beamforming design, with numerical examples given in Section VII. Finally, in Section VIII, we summarize, draw conclusions, and suggest further work.

Manuscript received January 27, 2001; accepted April 18, 2002. This work was sponsored principally by Grant No. HL 60301 from the National Institutes of Health, USA and partially by Grant No. 26-01-0178 from the Danish Science Foundation, Denmark (a few hours for reviewing the author proof).

P. Fox is with Ørsted·DTU, Technical University of Denmark, DK-2800 Lyngby, Denmark (e-mail: pdf@oersted.dtu.dk).

J. Cheng and J.-Y. Lu are with the Ultrasound Laboratory, Department of Bioengineering, University of Toledo, Toledo, OH 43606-3390 USA (e-mail: jilu@eng.utoledo.edu).

## II. Model Definitions

### A. Propagation Model

Annular arrays have circular symmetry around the propagation axis, for which we assume the governing circular symmetric linear wave equation

$$\left[\frac{1}{r}\frac{\partial}{\partial r}\left(r\frac{\partial}{\partial r}\right)+\frac{\partial^2}{\partial z^2}-\frac{1}{c^2}\frac{\partial^2}{\partial t^2}\right]f(r,z,t)=0 \qquad (1)$$

in which $f(r,z,t)$ is the field pressure relative to static pressure, $r$ is the radial distance from the cylindrical centerline, $z$ is the outward propagation distance perpendicular to the transducer surface (placed at $z=0$ and centered around $r=0$), and $c$ is the speed of sound (assumed real). For a given wavenumber $k=\omega/c$, this equation has Bessel beam solutions [4], [7] of the form

$$\begin{aligned} f(r,z,t) &= J_0(\alpha r)\cdot e^{j\beta z}\cdot e^{-j\omega t} \\ \alpha^2+\beta^2 &= k^2. \end{aligned} \qquad (2)$$

### B. Annular Arrays

We then consider $N$-ring flat annular arrays with monochromatic surface pressure $q(r,t) = q(r)e^{-j\omega t}$, in which $q(r)$ is the spatial quantization profile and $\omega$ is the angular frequency. In annular arrays, $q(r)$ is stepwise constant with discrete quantization values $q_p$, where

$p = 1, \ldots, N$ is the ring number, and $p = 1$ for the inner ring with $p = N$ for the outer ring. Inner and outer ring radii are denoted $r_p^-$ and $r_p^+$, respectively, with $r_1^- = 0$, $r_N^+ = R$ by definition and the kerf between successive rings being $r_p^- - r_{p-1}^+$. Relative time delays $\tau_p$ on each ring may also exist, allowing $q_p$ to take the complex form

$$q_p = \gamma_p + j\delta_p = |q_p|\, e^{j\theta_p} \tag{3}$$

such that each ring emits pressure $q_p e^{-j\omega t} = |q_p|\, e^{j\theta_p} e^{-j\omega t} = |q_p|\, e^{-j\omega(t-\tau_p)}$, where $|q_p|$, $\theta_p$, and $\tau_p$ are the respective ring magnitudes, phases, and time delays obtained from (3) as

$$|q_p| = \sqrt{\gamma_p^2 + \delta_p^2}, \quad \theta_p = -j\ln(q_p/|q_p|), \quad \tau_p = \theta_p/\omega. \tag{4}$$

## III. Use of 1-D Fourier-Bessel Series

### A. Application of Fourier-Bessel Series

We begin by applying 1-D Fourier-Bessel series [1], [2] to model the quantized surface pressure $q(r)$ as an infinite set of known basis Bessel functions. This series is defined by

$$\begin{aligned} q(r) &= \sum_{i=1}^{\infty} A_i \cdot J_0(\alpha_i r) \\ \alpha_i &= x_i/a, \quad J_0(x_i) = 0 \\ A_i &= \frac{2}{a^2 J_1^2(x_i)} \int_0^a q(r) \cdot J_0(\alpha_i r) r dr \end{aligned} \tag{5}$$

where $J_0(\cdot)$ is the Bessel function of the first kind of order zero, $A_i$ is the appropriate set of weighting coefficients, and the roots $x_i$ are the known infinite set of monotonically increasing positive solutions to $J_0(x_i) = 0$. The series in (5) is then valid over the radial range $0 \le r \le a$ , where $a$ is any desired modelling aperture subject to the constraint $q(a) = 0$, as $J_0(\alpha_i a) = 0$ by definition of $J_0(x_i) = 0$. (Note that for ease of discussion, we use the term aperture here to refer to the radial dimension $a$ and not the corresponding diameter $2a$).

### B. Interpretation of Fourier-Bessel Series

What the Fourier-Bessel series in (5) represents physically is that we may model both the quantized surface pressure $q(r)$ at $z = 0$ as $q_1 \ldots q_N$ over $N$ rings of the transducer in the range $0 \le a \le R$, and then as $q(r) = 0$ beyond the transducer surface $a > R$, as the (relative) surface pressure is zero by definition beyond the transducer edge. This satisfies the condition $q(a) = 0$ as required by the definition of the series. Then, $q(r)$ in (5) equates to a surface profile $q(r)e^{-j\omega t} = \sum_{i=1}^{\infty} A_i \cdot J_0(\alpha_i r) \cdot e^{-j\omega t}$, and, if this profile is implemented over an infinite aperture ($a \to \infty$), each component $i$ represents an exact nondiffracting Bessel beam solution [4], [7] at the transducer surface $z = 0$ to the wave (1). The general propagating solution for $z > 0$ is then $A_i \cdot J_0(\alpha_i r) \cdot e^{j\beta_i z} \cdot e^{-j\omega t}$, and the total field $f(r, z, t)$ may therefore be defined as the sum of all of these components, namely

$$\begin{aligned} f(r, z, t) &= \lim_{a\to\infty} \sum_{i=1}^{\infty} A_i \cdot J_0(\alpha_i r) \cdot e^{j\beta_i z} \cdot e^{-j\omega t} \\ \beta_i &= \sqrt{k^2 - \alpha_i^2} \end{aligned} \tag{6}$$

in which $k = \omega/c$ is the wavenumber, the real parameter $\alpha_i \ge 0$ is the scaling parameter in the $r$ direction, and $\beta_i$ is the component in the $z$ direction. In addition, because the positive Bessel roots $x_i \approx \pi i - \pi/4$ in (5) increase monotonically with index $i$, the corresponding $\alpha_i = x_i/a$ terms in (6) also increase monotonically for a given value of $a$. This causes a change in propagation characteristics for the distinct cases $\alpha_i \le k$ and $\alpha_i > k$. Because the wavenumber $k$ is assumed real, then $\beta_i$ is purely real when $\alpha_i \le k$ and all corresponding components $A_i \cdot J_0(\alpha_i r) \cdot e^{j\beta_i z} \cdot e^{-j\omega t}$ propagate to infinity in the $z$ direction for $z > 0$. However, when $\alpha_i > k$, the values $\beta_i$ become purely imaginary, and these propagate as $A_i \cdot J_0(\alpha_i r) \cdot e^{-|\beta_i| z} \cdot e^{-j\omega t}$, which is to say with exponential decay in the $z > 0$ direction. These are evanescent beam components, which are usually all negligible, as the magnitudes of $|\beta_i|$ involved typically cause the beam amplitudes $A_i \cdot J_0(\alpha_i r) \cdot e^{-|\beta_i| z}$ to decay to negligible levels within the first few wavelengths of the transducer surface.

## IV. Theory for Field Computation

### A. Computation Mechanism

Therefore, if we define $l(k, a)$ as the number of nonnegligible (generally exclusively nonevanescent) components for a given application, the original infinite sum in (6) effectively becomes replaced by the truncated finite sum

$$f(r, z, t) = \lim_{a\to\infty} \sum_{i=1}^{l(k,a)} A_i \cdot J_0(\alpha_i r) \cdot e^{j\beta_i z} \cdot e^{-j\omega t}, \quad z > 0 \tag{7}$$

in which all required parameters $A_i$, $\alpha_i$, $\beta_i$ are now known from (5) and (6). Further, from the root approximation $x_i \approx \pi i - \pi/4$ and the definition $\alpha_i = x_i/a$, we have $\alpha_i a \approx \pi i - \pi/4$. Hence, the coefficient index $i = l(k, a)$ at which the swap between nonevanescent and evanescent characteristics occurs ($\alpha_i = k$) is given by

$$l(k, a) \approx ka/\pi + 1/4. \tag{8}$$

Note that this is independent of the surface pressure profile $q(r)$, but proportional to both wavenumber $k$ and modelling aperture $a$. Therefore, implementing $a \to \infty$ in (7) causes $l(k, a) \to \infty$, and, hence, in theory at least, we still need to sum an infinite number of terms to compute $f(r, z, t)$ exactly. Clearly, this is not possible from a practical point of view, but it is possible is to iterate $a$ toward infinity in (7) and wait for the corresponding field calculations $f(r, z, t)$ to converge to within an acceptable level. Typically, we might use $a = 10R$, $a = 20R$, $a = 30R$, and so on, until the maximum change in field intensity between successive $a$ values drops either to within a given number of decibels, or a given relative percentage (e.g., 0.1%). See Section V for a detailed numerical example of computing the field.

### B. Numerical Aspects

For annular arrays as per Section II-B, the integral for the weighting coefficients $A_i$ in (5) may be evaluated piecewise over the $N$ rings $p = 1, \ldots, N$ to give

$$
\begin{aligned}
A_i &= \sum_{p=1}^{N} C_{i,p} \cdot q_p \\
C_{i,p} &= 2\left[r_p^+ J_1(\alpha_i r_p^+) - r_p^- J_1(\alpha_i r_p^-)\right] / a x_i J_1^2(x_i)
\end{aligned} \tag{9}
$$

where $J_1(\cdot)$ is the first-order Bessel function of the first kind. The coefficients $A_i$ are, therefore, generally complex, as $C_{i,p}$ is real by definition, but $q_p$ are complex according to Section II-B. Notice also that all coefficients $C_{i,p}$ are functions of geometry only, and need only be computed once for a given transducer layout, as they are independent of the ring pressures $q_p$. One may then also employ the approximations

$$
\begin{aligned}
J_0(x) &\approx \sqrt{2/\pi x} \cdot \cos(x - \pi/4), \quad x \geq 1 \\
J_1(x) &\approx \sqrt{2/\pi x} \cdot \cos(x - 3\pi/4), \quad x \geq 2
\end{aligned} \tag{10}
$$

from [1] to obtain the roots $x_i$ to $J_0(x_i) = 0$ as $x_i \approx \pi i - \pi/4$, and, hence, $J_1(x_i) \approx \sqrt{2/\pi x_i}$, leading to $a x_i J_1^2(x_i) \approx 2a/\pi$ and hence

$$
C_{i,p} \approx \pi\left[r_p^+ J_1(\alpha_i r_p^+) - r_p^- J_1(\alpha_i r_p^-)\right] / a \tag{11}
$$

which shows that $|C_{i,p}|$ is bounded for all finite $r_p^+$, $r_p^-$, $a$ and all $i$, as $|J_1(\cdot)| < 0.6$ by definition. In fact, $|C_{i,p}| \to 0$ as $\alpha_i \to \infty$, because $\alpha_i \to \infty$ as $i \to \infty$ and $|J_1(x)| \to 0$ as $x \to \infty$ by definition. Therefore, $|A_i| \to 0$ as $\alpha_i \to \infty$ because all ring values $q_p$ are fixed and finite. Note also two further numerical features. First, from (11) and (9) $|A_i|$ decreases with increasing $a$, as $|C_{i,p}|$ decreases with increasing $a$ for a fixed value of $i$. Second, because the monotonically increasing Bessel root values $x_i$ are given by $x_i \approx \pi i - \pi/4$, then $x_i - x_{i-1} \approx \pi$, and, hence, consecutive alpha parameters in the series are spaced by an amount $\alpha_i - \alpha_{i-1} = (x_i - x_{i-1})/a \approx \pi/a$. This spacing decreases with increasing $a$, and an increasing number of nonevanescent alpha parameters appear in the nonevanescent region $\alpha_i \leq k$ as $a$ is increased. It is also the reason why $l(k, a) \to \infty$ as $a \to \infty$ because then $\alpha_i - \alpha_{i-1} \to 0$ and an infinite number of $\alpha_i$ parameters appear in a finite interval $0 < \alpha_i \leq k$.

Notice also that implementing $a > R$ is equivalent to considering an equivalent transducer with $N' = N + 1$ rings, in which the outer ring has quantization level $q_{N'} = q_{N+1} = 0$, inner radius $r_{N+1}^- = r_N^+ = R$, and outer radius $r_{N+1}^+ = a$. Theoretically, this gives rise to a new sum $A_i = \sum_{p=1}^{N'=N+1} C_{i,p} \cdot q_p$ in place of $A_i = \sum_{p=1}^{N} C_{i,p} \cdot q_p$ in (9), but because $q_{N'} = 0$ by definition, the sum remains fixed in practice at that given in (9). However, the $C_{i,p}$ coefficients change in (9) through their dependence on $a$, and, therefore, different $A_i$ weighting distributions are obtained for different values of $a$. (See the plots supplied in Section V for a full illustration.)

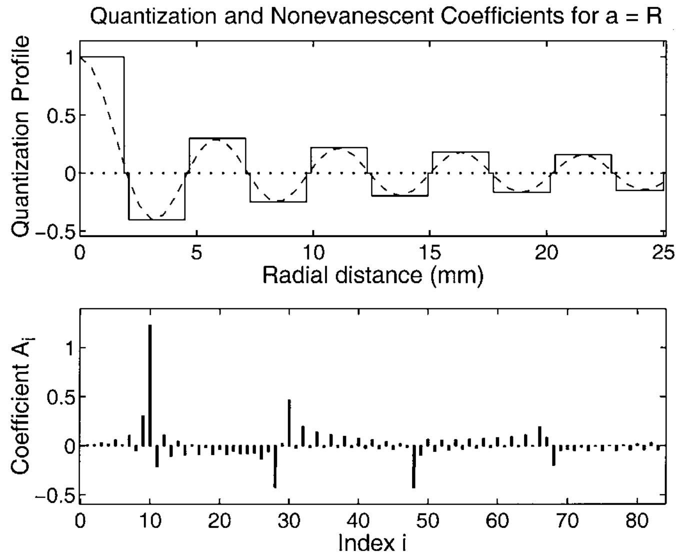


Fig. 1. Quantization profile (upper) and nonevanescent Fourier-Bessel coefficients $A_i$ (lower) for modelling aperture $a = R$.

## V. Example of Field Computation

In this section, we illustrate the Fourier-Bessel method numerically and compare it with both experimental field results and Rayleigh-Sommerfeld simulations with Fresnel approximations.

### A. Transducer Definition

Consider the Bessel transducer of Lu and Greenleaf described in [5]. The transducer is an $N = 10$-ring Bessel-design transducer whose ring edges are located nominally at the first 10 zeros of $J_0(\alpha r)$, where $\alpha = 1202.45\ \mathrm{m}^{-1}$. In practice, the transducer has kerf of approximately 0.2 mm, such that in terms of the notation of Section II-B, $r_1^- = 0$, $r_1^+ = x_1/\alpha - \mathrm{kerf}/2$, $r_2^- = x_1/\alpha + \mathrm{kerf}/2$, and so on. Operating conditions are $f = 2.5$ MHz in water at speed of sound $c = 1500$ m/s, giving wavenumber $k = 10471.98\ \mathrm{m}^{-1}$. The $R = 25$-mm transducer has its ring pressures $q_p$ (solid lines in Fig. 1, upper) chosen as the peak value of each respective Bessel lobe (dashed line in Fig. 1, upper).

### B. Illustration of Field Convergence

The convergence principle for the field calculation as $a \to \infty$ is illustrated in Fig. 1 through 5. Beginning with

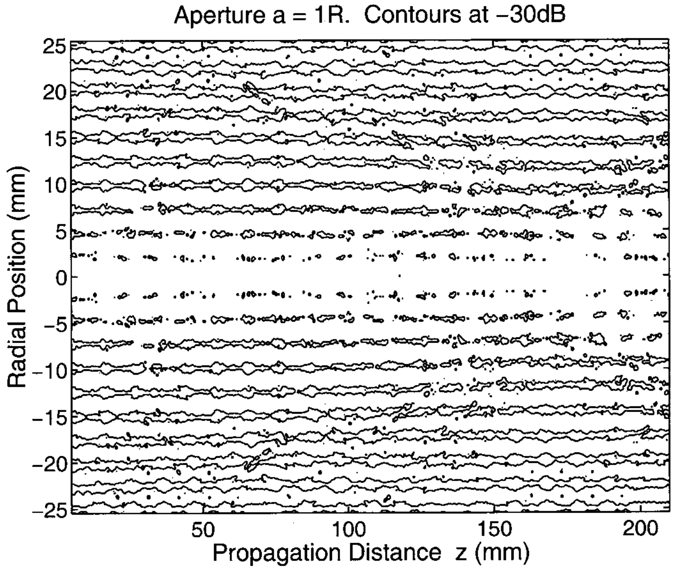


Fig. 2. −30 dB contour levels for field calculation with $a = R$.

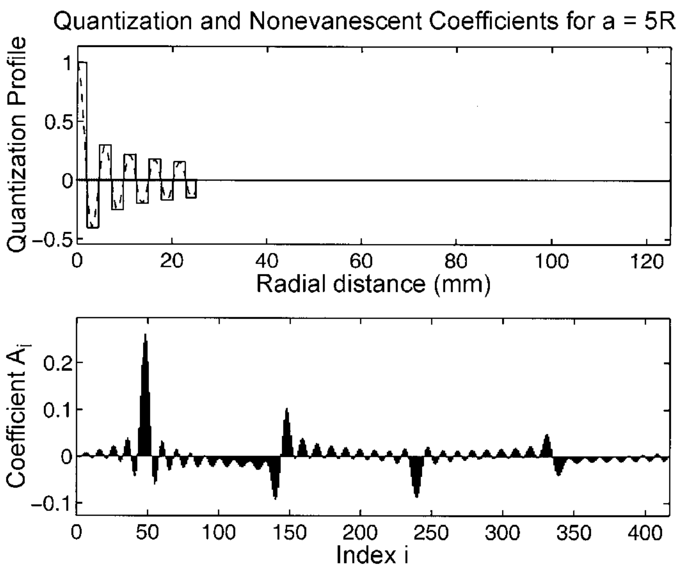


Fig. 3. Quantization profile (upper) and nonevanescent Fourier-Bessel coefficients $A_i$ (lower) for modelling aperture $a = 5R$.

$a = R = 25$ mm, we obtain $l(k, a) = 83$ nonevanescent $A_i$ coefficients, as shown in Fig. 1 (lower). See [16] and [9] for a full discussion of the significance of the different $A_i$ weightings and their associated field components. The calculation field based on $a = R$ is then shown in Fig. 2, where the lines shown represent the calculated −30 dB field contours. Note that we do not yet assume this to be the true field because we have not yet begun the iteration process of allowing $a \to \infty$. In Fig. 3 and 4, we then show the corresponding results for modelling aperture $a = 5R = 125$ mm. In this case, there are $l(k, a) = 416$ nonevanescent $A_i$ coefficients as shown in Fig. 3 (lower). Notice that the number of coefficients has increased while the relative magnitudes have decreased as $a$ has been increased; both these properties were predicted by the discussion given in Section IV-B.

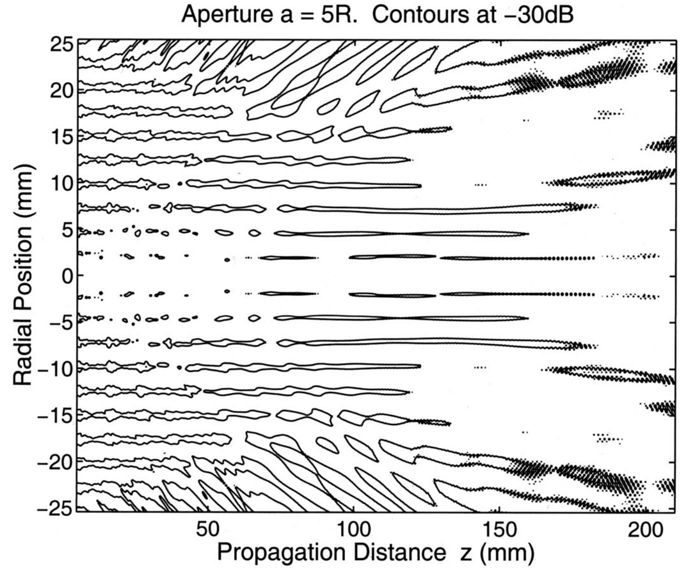


Fig. 4. −30 dB contour levels for field calculation with $a = 5R$.

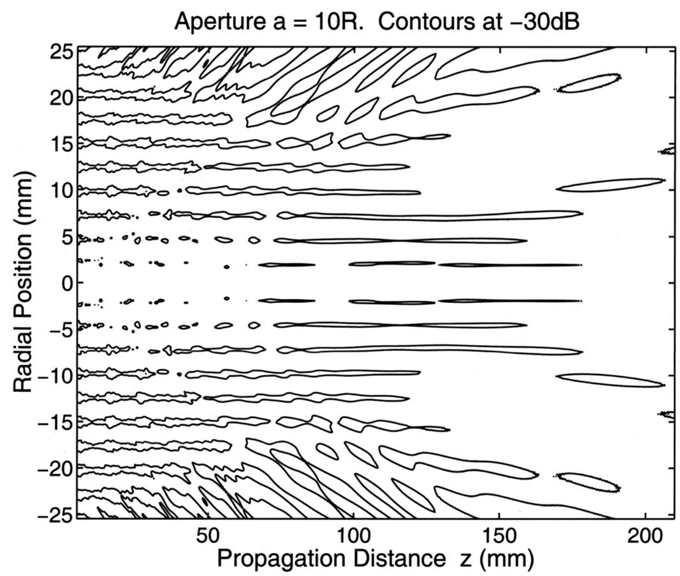


Fig. 5. −30 dB contour levels for field calculation with $a = 10R$.

The −30 dB field plot in Fig. 4 has also changed considerably with respect to Fig. 2, and so the modelling aperture is then increased to $a = 10R = 250$ mm for which $l(k, a) = 833$, and the corresponding field plot is given in Fig. 5. This plot has changed much less than was the case previously, indicating that the convergence of the field calculation has begun to take place. As the aperture is increased to $a = 20R$ and $a = 30R$, no further visible changes are apparent in the −30 dB plots, and the maximum relative change in field intensity encountered anywhere in the entire region of interest is found to drop to within less than 1%. For practical purposes, we consider convergence to have taken place at $a = 30R = 750$ mm for which $l(k, a) = 2500$ coefficients. (See Table I for a fuller set of field parameters as a function of modeling aperture

TABLE I
FIELD CALCULATION PARAMETERS AS A FUNCTION OF INCREASING APERTURE RATIO.

| Aperture ratio | $a = R$ | $a = 5R$ | $a = 10R$ | $a = 20R$ | $a = 30R$ |
|---|---|---|---|---|---|
| Number of nonevanescent coefficients | 83 | 416 | 833 | 1666 | 2500 |
| Maximum relative field intensity change present (%) | — | 82.65 | 15.69 | 1.93 | 0.79 |
| Maximum field intensity present (dB) | 10.74 | 9.48 | 9.48 | 9.48 | 9.48 |
| Minimum field intensity present (dB) | −92.55 | −84.41 | −72.34 | −74.32 | −73.44 |

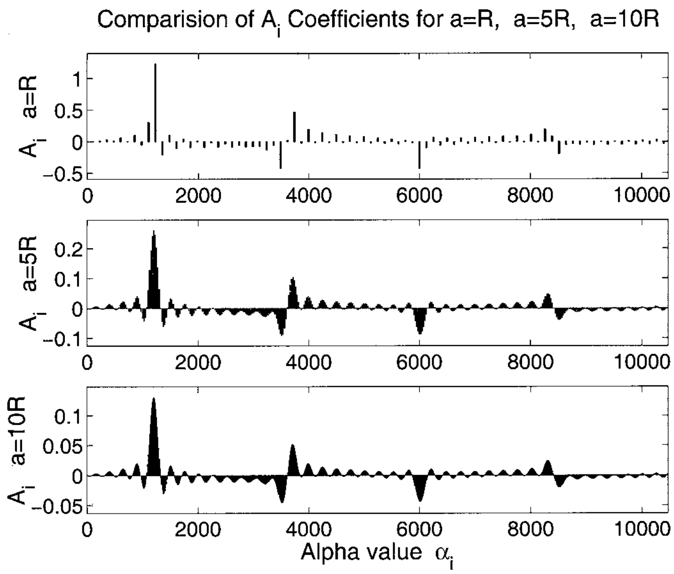


Fig. 6. Nonevanescent coefficient values $A_i$ versus alpha values $\alpha_i$ for $a = R$, $a = 5R$, $a = 10R$ and wavenumber $k = 10\,471.98$ m$^{-1}$.

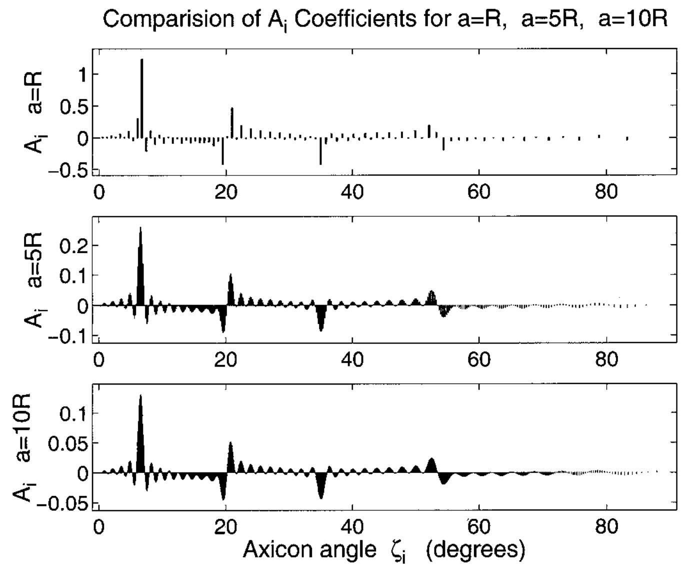


Fig. 7. Nonevanescent coefficient values $A_i$ versus axicon angles $\zeta_i = \sin^{-1}(\alpha_i/k)$ for $a = R$, $a = 5R$, $a = 10R$ and wavenumber $k = 10\,471.98$ m$^{-1}$.

$a$). Finally, in Fig. 6 and 7, respectively, the $A_i$ coefficients are plotted against $\alpha_i$ and corresponding axicon angles $\zeta_i = \sin^{-1}(\alpha_i/k)$ for the three first apertures $a = R$, $a = 5R$, $a = 10R$. As commented previously, the coefficient magnitudes decrease as the number of nonevanescent coefficients increase with increasing $a$. However, what appears to remain constant is the shape (although not magnitude) of the envelope of the field component distributions, suggesting that in the limit of $a \to \infty$, the field becomes expressed by an infinite number of subfields weighted primarily around particular values of $\alpha$ and corresponding axicon angles $\zeta$. Moreover, these principle values appear to be the principal limited diffraction field components already analyzed recently in [16].

### C. Comparison with Experimental and Rayleigh-Sommerfeld Results

Fig. 8(a) shows the greyscale image of the transducer field evaluated with $a = 30R$. Next to it in Fig. 8(b), we see the excellent agreement with the experimental field result of [5]. Fig. 8(c) then shows the Rayleigh-Sommerfeld field computation without Fresnel approximation, which again agrees very closely with the Fourier-Bessel calculation. Finally, in Fig. 8(d), we show the Rayleigh-Sommerfeld computation without Fresnel approximation, which suffers from errors in the very nearfield. Notice that these errors are absent in the Fourier-Bessel calculation. In addition to its accuracy, the Fourier-Bessel algorithm ran 14.1 and 3844.3 times faster than the Rayleigh-Sommerfeld algorithms with and without Fresnel approximations, respectively (see Table II).

## VI. Theory for Tuning

### A. Computation Mechanism

The theory for tuning of annular arrays using Fourier-Bessel series has already been outlined in [15] in the context of tuning a Bessel beam on an equal area annular array. Here, we first review it and then apply it more extensively than previously for a different type of array in Section VII. The field $f(r, z, t)$ in (7) may be separated into the product of time component $e^{-j\omega t}$ and spatial component $f(r, z)$ in terms of the ring pressures $q_p = \gamma_p + j\delta_p$ by combining (7), (9), and (3) to obtain

$$f(r,z,t) = e^{-j\omega t} \cdot \lim_{a\to\infty} \sum_{i=1}^{l(k,a)} J_0\left(\frac{x_i r}{a}\right) \times \left[\sum_{p=1}^{N} C_{i,p} \cdot e^{j\beta_i z} \cdot (\gamma_p + j\delta_p)\right] = e^{-j\omega t} \cdot f(r,z) \quad (12)$$

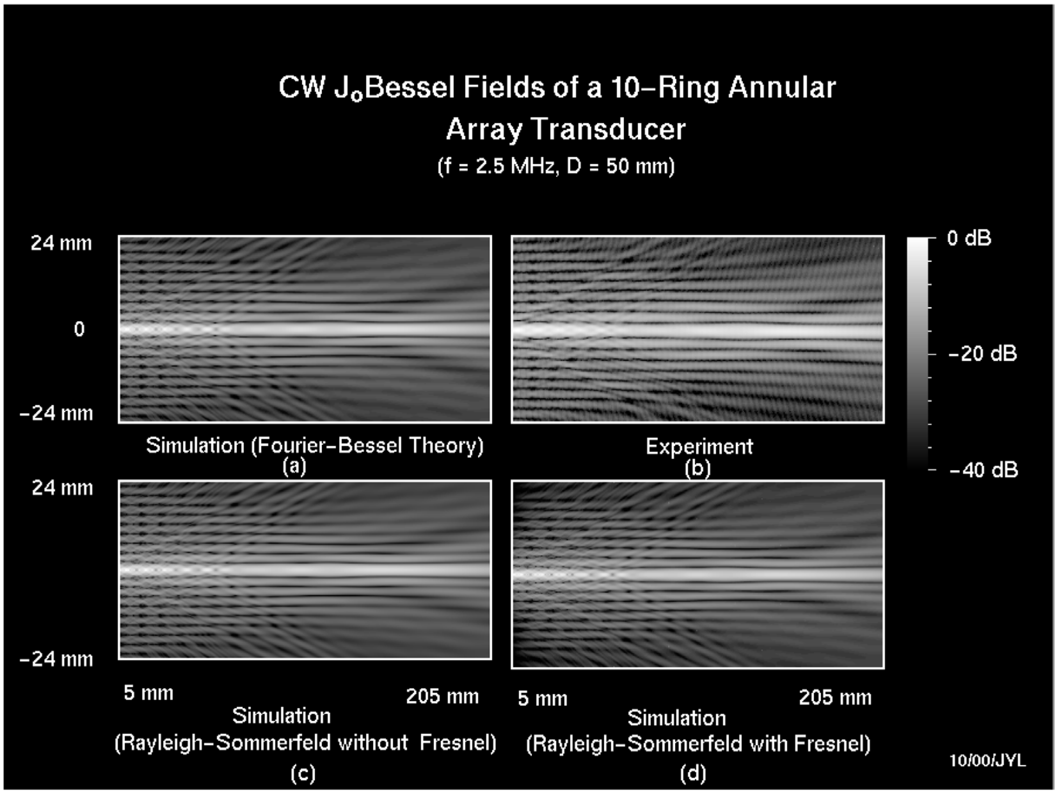


Fig. 8. Field for quantized CW Bessel beam. a) Field calculated by Fourier-Bessel theory. b) Experimental field. c) Field calculated by Rayleigh-Sommerfeld formula without Fresnel approximation. d) Field calculated by Rayleigh-Sommerfeld formula with Fresnel approximation.

TABLE II
Comparison of Relative Run Times for Different Field Simulation Methods.

| Simulation method | Fourier-Bessel | Rayleigh-Sommerfeld with Fresnel | Rayleigh-Sommerfeld without Fresnel |
|---|---|---|---|
| Time (h:min:s) | 00:00:28 | 00:06:35 | 29:54:00 |
| Time (s) | 28 | 395 | 107 640 |
| Time (relative) | 1 | 14.1 | 3844.3 |

The spatial field component $f(r,z)$ postmultiplying $e^{-j\omega t}$, therefore, has complex form $f(r,z) = f^{\Re}(r,z) + jf^{\Im}(r,z)$, where $f^{\Re}(r,z)$ and $f^{\Im}(r,z)$ are the real and imaginary components, respectively. From this, the field at all points of interest $r = r_u$, $z = z_v$ ($u = 1 \ldots n_u$ and $v = 1 \ldots n_v$) may be written as (13) (see next page) in which $M^{\Re}_{i,p,v}$ and $M^{\Im}_{i,p,v}$ are the real and imaginary parts of the product $M_{i,p,v} = C_{i,p} \cdot e^{j\beta_i z_v}$, respectively. Eq. (13) then has block form

$$F = MQ \tag{14}$$

in which

$$Q = [\gamma_1, \delta_1, \ldots, \gamma_N, \delta_N]' \tag{15}$$

on the right-hand side is the vector containing the real and imaginary parts of all $N$ adjustable ring pressures $q_1, \ldots, q_N$. This vector has dimension $Q = Q\{2N, 1\}$, where the notation $Q\{\text{rows, cols}\}$ indicates the number of rows and columns, respectively.

We then aim to minimize the envelope of the difference in field intensity between the actual field vector $F = F\{2n_u n_v, 1\}$ and some desired field vector $D = D\{2n_u n_v, 1\}$ in a least squares sense by adjusting all components $\gamma_1, \delta_1, \ldots, \gamma_N, \delta_N$ from the ring pressures in (3) appropriately. To achieve this, first define the desired field $d(r,z,t) = e^{-j\omega t} \cdot d(r,z)$ as a product of time component $e^{-j\omega t}$ and spatial component $d(r,z)$. The real and imaginary spatial components $d^{\Re}(r_u, z_v)$, $d^{\Im}(r_u, z_v)$ may then be written out at all points of interest ($u = 1 \ldots n_u$ and $v = 1 \ldots n_v$) in the same format as the vector $F$, i.e. (16) (see next page) and the least squares minimization problem with respect to $Q$ then reduces to the minimization of the error sum $S = [F - D]'[F - D]$. Substituting $F = MQ$

$$\begin{bmatrix} f^{\Re}(r_1, z_1) \\ f^{\Im}(r_1, z_1) \\ \vdots \\ f^{\Re}(r_u, z_v) \\ f^{\Im}(r_u, z_v) \\ \vdots \\ f^{\Re}(r_{n_u}, z_{n_v}) \\ f^{\Im}(r_{n_u}, z_{n_v}) \end{bmatrix} = \begin{bmatrix} \lim\limits_{a\to\infty} \sum\limits_{i=1}^{l(k,a)} J_0\left(\frac{x, r}{a}\right) \begin{bmatrix} +M^{\Re}_{i,1,1}, -M^{\Im}_{i,1,1}, \dots, +M^{\Re}_{i,N,1}, -M^{\Im}_{i,N,1} \\ +M^{\Im}_{i,1,1}, +M^{\Re}_{i,1,1}, \dots, +M^{\Im}_{i,N,1}, +M^{\Re}_{i,N,1} \end{bmatrix} \\ \vdots \\ \lim\limits_{a\to\infty} \sum\limits_{i=1}^{l(k,a)} J_0\left(\frac{x_i r_u}{a}\right) \begin{bmatrix} +M^{\Re}_{i,1,v}, -M^{\Im}_{i,1,v}, \dots, +M^{\Re}_{i,N,v}, -M^{\Im}_{i,N,v} \\ +M^{\Im}_{i,1,v}, +M^{\Re}_{i,1,v}, \dots, +M^{\Im}_{i,N,v}, +M^{\Re}_{i,N,v} \end{bmatrix} \\ \vdots \\ \lim\limits_{a\to\infty} \sum\limits_{i=1}^{l(k,a)} J_0\left(\frac{x_i r_{n_u}}{a}\right) \begin{bmatrix} +M^{\Re}_{i,1,n_v}, -M^{\Im}_{i,1,n_v}, \dots, +M^{\Re}_{i,N,n_v}, -M^{\Im}_{i,N,n_v} \\ +M^{\Im}_{i,1,n_v}, +M^{\Re}_{i,1,n_v}, \dots, +M^{\Im}_{i,N,n_v}, +M^{\Re}_{i,N,n_v} \end{bmatrix} \end{bmatrix} \begin{bmatrix} \gamma_1 \\ \delta_1 \\ \vdots \\ \gamma_N \\ \delta_N \end{bmatrix} \tag{13}$$

$$D = \left[d^{\Re}(r_1, z_1), d^{\Im}(r_1, z_1), \dots, d^{\Re}(r_u, z_v), d^{\Im}(r_u, z_v), \dots, d^{\Re}(r_{n_u}, z_{n_v}), d^{\Im}(r_{n_u}, z_{n_v})\right]', \tag{16}$$

from (14) and minimizing with respect to $Q$ gives least squares solution $Q = Q_{ls}\{2N, 1\}$ as

$$Q_{ls} = [M'M]^{-1} M' \cdot D. \tag{17}$$

Note that this tuning method has some similarities to the previous limited diffraction design of [17], but possesses two major differences in approach and objective. The first is that [17] considers a single value of $\alpha$ and then combines weightings of $J_n(\alpha)$ for different Bessel orders $n$, whereas this method considers multiple values of $\alpha_i$ but combines weightings of $J_n(\alpha_i)$ for $n = 0$ only. The second is that [17] derives weighting parameters on the assumption that the resulting Bessel functions could be realized perfectly in practice on the transducer surface, whereas this method considers specifically the effects of quantization on the transducer and derives a tuning scheme that takes these restrictions into account.

### *B. Numerical Aspects*

The vector dimensions $F = F\{2n_u n_v, 1\}$ and $Q = Q\{2N, 1\}$ cause the large matrix $M$ premultiplying $Q$ to have dimension $M = M\{2n_u n_v, 2N\}$ and the inverse $[M'M]^{-1}$ in (17) must exist for the solution to be realizable. Hence, $M'M = M'M\{2N, 2N\}$ must have full rank $2N$, and this imposes a requirement of $n_u n_v \geq N$ to prevent $M$ (and thereby $M'M$) from being rank deficient for dimensional reasons. In addition, consideration needs to be given to spatial sampling rates. From (7), component $i$ of the sum propagates in the $z$ direction as $e^{j\beta_i z}$ with wavelength $2\pi/\beta_i$ for the nonevanescent components. The shortest possible wavelength is, therefore, that corresponding to the maximum possible nonevanescent value of $\beta_i$, namely $\beta_{\max} = k$ when $\alpha_i = 0$ in (6). This gives a wavelength of $2\pi/k$, which, to comply with the Shannon sampling theorem, dictates a sampling interval in the $z$ direction of $\pi/k$ or lower. In the radial direction $r$, the approximation $J_0(\alpha_i r) \approx \sqrt{2/\pi\alpha_i r} \cdot \cos(\alpha_i r - \pi/4)$ from (10) allows us to approximate the radial oscillations as a cosine function of wavelength $2\pi/\alpha_i$. The minimum wavelength possible is then also $2\pi/k$, corresponding to the maximum nonevanescent value $\alpha_i = k$ possible in (6). Therefore, this also leads to a sampling interval of $\pi/k$ or lower in the $r$ direction. Finally, we also need, in practice, to iterate for different values of $M$ for $a \to \infty$, calculate $Q_{ls}$ for each value of $a$, and wait for the corresponding quantization magnitudes $|q_p|$ and phases $\theta_p$ or time delays $\tau_p$ from (4) to converge to within acceptable levels. (See Section VII for a full numerical example).

## VII. Examples of Tuning

For tuning examples, we consider the focusing of a Gaussian beam with focal length $F = 120$ mm on the given annular array. This is obtained initially without any least squares tuning by quantizing both the ring amplitudes $|q_p|$ and phases $\theta_p$ (3) over each annulus according to

$$q_p = e^{-r_p^2/\sigma^2} \cdot e^{jk\left(F - \sqrt{F^2 + r_p^2}\right)} = |q_p|\, e^{j\theta_p}, \tag{18}$$

which is a discretized version of the Gaussian surface pressure expression given in [5] in which $r_1 = 0$, $r_p = (r_p^- + r_p^+)/2$, $(p = 2 \dots 10)$, $\sigma = 15$ mm, $F = 120$ mm, and $k = 10.4798$ mm$^{-1}$. Eq. (18) gives amplitudes and phases as per rows 1 and 2 in Table III, for which all $A_i$ coefficients are imaginary, as all $q_p$ are imaginary.

### *A. Experimental Gaussian Field*

The Fourier-Bessel field calculation with $a = 30R$ for (18) leads to the field in Fig. 9(a) over the intervals $0 \leq r \leq 24$ mm and $5 \leq z \leq 210$ mm. The result demonstrates a focus around $z = 120$ mm as expected, along with some nearfield diffraction in the region of $z < 100$ mm. We now compare this with the experimental result obtained previously in [5], whereby the array was quantized with the same discrete magnitudes $|q_p| = e^{-r_p^2/\sigma^2}$ as per (18) but, in

TABLE III
Quantization Amplitudes and Phases for Panels in Fig. 9(a) and 10(a and b).

| | Ring Number | | | | | | | | | |
|---|---|---|---|---|---|---|---|---|---|---|
| | $p = 1$ | $p = 2$ | $p = 3$ | $p = 4$ | $p = 5$ | $p = 6$ | $p = 7$ | $p = 8$ | $p = 9$ | $p = 10$ |
| $\lvert q_p \rvert$ Fig. 9(a) | 1.000 | 0.953 | 0.857 | 0.726 | 0.578 | 0.434 | 0.306 | 0.203 | 0.127 | 0.079 |
| $\theta_p/\pi$ Fig. 9(a) | 0 | −0.151 | −0.482 | −1.003 | −1.711 | −2.607 | −3.689 | −4.955 | −6.404 | −7.910 |
| $\lvert q_p \rvert$ Fig. 10(a) | 1.001 | 0.956 | 0.860 | 0.726 | 0.578 | 0.434 | 0.306 | 0.204 | 0.127 | 0.079 |
| $\theta_p/\pi$ Fig. 10(a) | −0.001 | −0.151 | −0.482 | 0.998 | 0.289 | −0.607 | 0.311 | −0.955 | −0.404 | 0.090 |
| Unwrapped | | | | 0.998−2 | 0.289−2 | −0.607−2 | 0.311−4 | −0.955−4 | −0.404−6 | 0.090−8 |
| $\theta_p/\pi - 2 * int$ | | | | = −1.002 | = −1.711 | = −2.607 | = −3.689 | = −4.955 | = −6.404 | = −7.910 |
| $\lvert q_p \rvert$ Fig. 10(b) | 1.007 | 0.959 | 0.862 | 0.726 | 0.578 | 0.434 | 0.305 | 0.202 | 0.126 | 0.077 |
| $\theta_p/\pi$ Fig. 10(b) | −0.001 | −0.152 | −0.482 | 0.998 | 0.289 | −0.607 | 0.311 | −0.955 | −0.404 | 0.092 |
| Unwrapped | | | | 0.998−2 | 0.289−2 | −0.607−2 | 0.311−4 | −0.955−4 | −0.404−6 | 0.092−8 |
| $\theta_p/\pi - 2 * int$ | | | | = −1.002 | = −1.711 | = −2.607 | = −3.689 | = −4.955 | = −6.404 | = −7.908 |

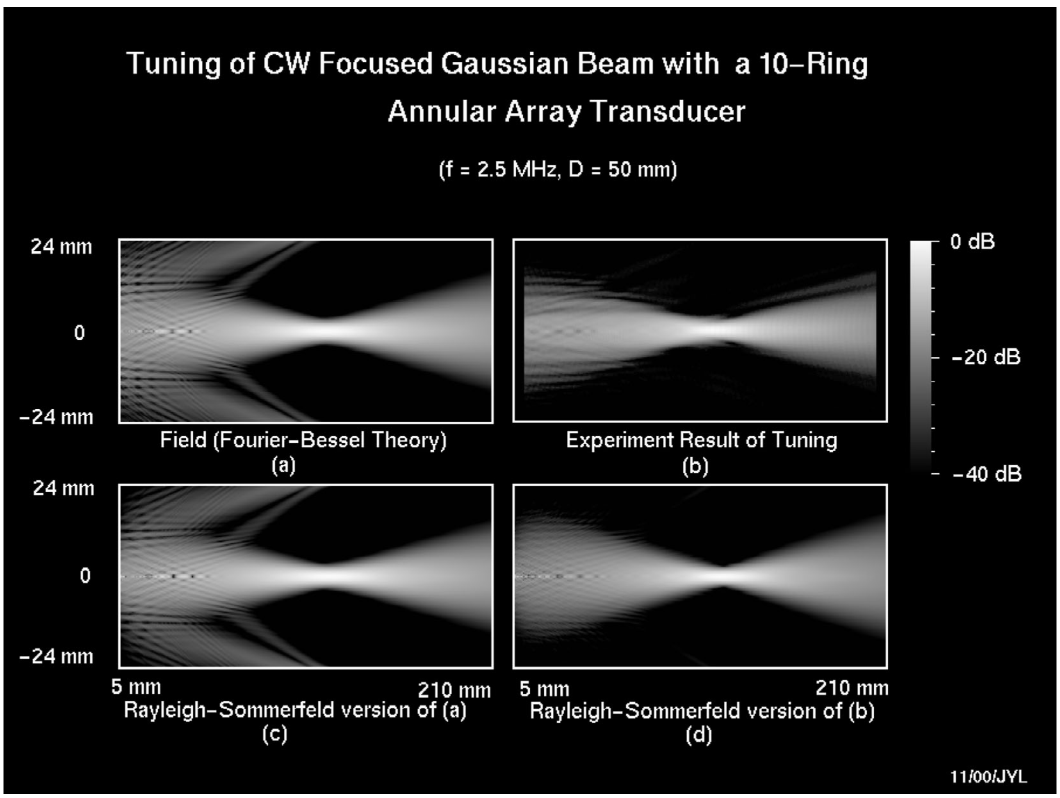


Fig. 9. Tuning results for a CW focused Gaussian beam. a) Focused Gaussian beam field calculated with Fourier-Bessel theory. b) Experimental tuning using an acoustic lens. c) Rayleigh-Sommerfeld verification of (a). d) Rayleigh-Sommerfeld verification of (b).

practice, with continuous phases $\theta(r) = k(F - \sqrt{F^2 + r^2})$ obtained by placing an acoustic lens across the surface of the transducer (see [5] for details). The resulting experimental field is given in Fig. 9(b), demonstrating an almost identical focus to Fig. 9(a), but this time without the diffraction for $z < 100$ mm. This difference appears to be due to the difference between the quantized phases in Fig. 9(a) and the continuous phases in Fig. 9(b). To verify that this is the case as opposed to any simulation error in the Fourier-Bessel method for the case of complex ring pressures, we then also simulate the fields for both Fig. 9(a and b) using the Rayleigh-Sommerfeld diffraction formula. The results are given in Fig. 9(c and d), respectively, demonstrating that both Fig. 9(a and b) are indeed consistent with the independent Rayleigh-Sommerfeld method; therefore, the Fourier-Bessel simulation method for complex ring pressures still holds good.

### *B. Verification of Tuning Algorithm Using Gaussian Field*

Therefore, with full confidence in the Fourier-Bessel field evaluation method and taking Fig. 9(a) as the benchmark for what we know may be achieved given the constraints of discretized quantization phases, we now consider how the array could be tuned using that desired field but in the absence of the underlying (18). First, we take

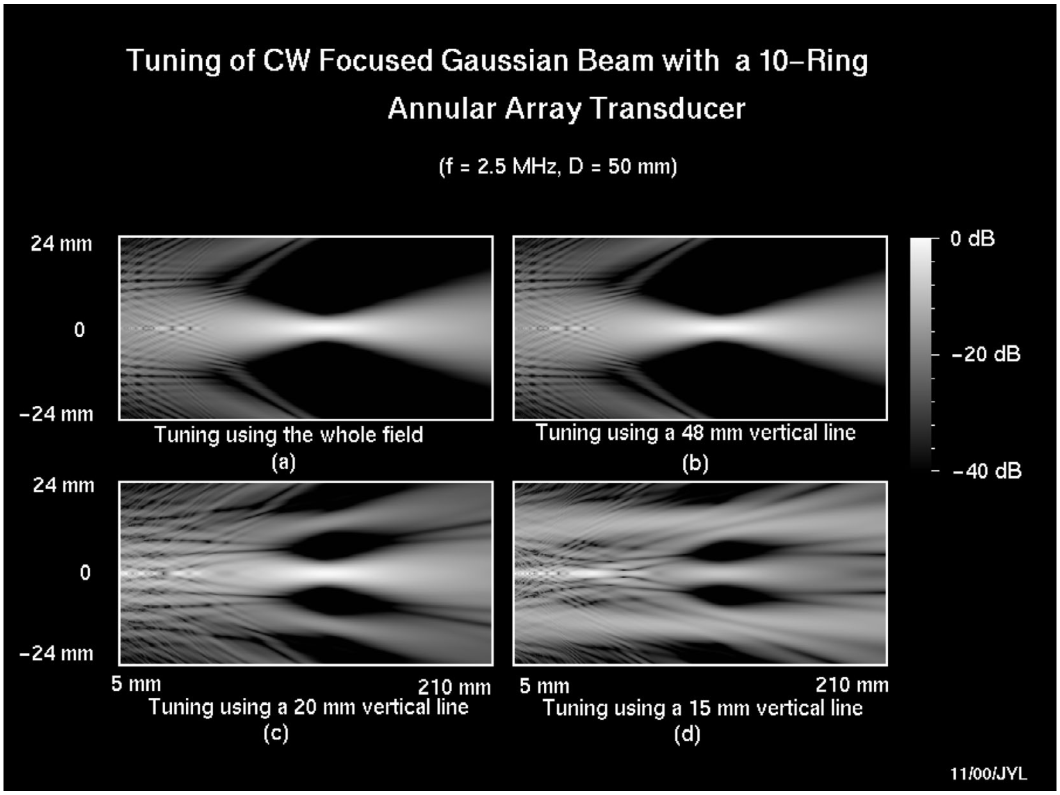


Fig. 10. Tuning results for a CW focused Gaussian beam. (a) Tuning result using the whole field Fig. 9(a). b) Tuning result using a 48-mm vertical line of the field in Fig. 9(a) through the focal distance $z = F = 120$ mm. c) Same as (b) but with vertical line of 20 mm. d) Same as (b) but with vertical line of 15 mm.

the entire field in Fig. 9(a) to construct the desired field vector $D$ in (16), (17), and apply the tuning algorithm of Section VI with lateral ($r$) and axial ($z$) resolutions of 0.3 mm each. (Notice that these comply with the required sampling intervals of $\pi/k = 0.30$ mm or lower derived in Section VI. If the tuning theory is correct, we should then expect to retrieve the exact quantization magnitudes and phases that generated this field, as the tuning is recreating a field that we already know. In practice, we do indeed find this to be the case, with the least squares ring pressures and phases (rows 3 and 4 of Table III) being virtually identical to the original phases (rows 1 and 2 of Table III). The field for the subsequent least squares ring pressures is given in Fig. 10(a); compare this with the original given field in Fig. 9(a). Hence, we have now established that both the field calculation and tuning methods are valid and accurate.

### *C. Tuning Using Reduced Gaussian Field*

A drawback, however, is that the tuning algorithm takes a long time to run when using the entire field data (approximately 6 h on a 600-MHz Pentium III PC programmed in C). So we now investigate how well it performs when substituting a much smaller slice of field data for the desired vector $D$. To do this, take only a single line of the field data sampled across the 48-mm radial cross-section of interest ($0 \leq r \leq 24$ mm) in the plots at the focal distance $z = 120$ mm. The computation time is then reduced to only a few minutes while the ring pressures are still found to be retrieved satisfactorily [see rows 5 and 6 of Table III and the corresponding field plot in Fig. 10(b). We then attempt to reduce the data set even further by sampling first only the first 20 mm ($0 \leq r \leq 10$ mm) and second only the first 15 mm ($0 \leq r \leq 7.5$ mm) symmetrically around the central axis $r = 0$ at $z = 120$ mm from Fig. 9(a) [see Fig. 10(c and d), respectively]. Here, we see a degradation in the desired field because of the appearance of unwanted sidelobes on either side of the central focal zone. The reason for this is that, in specifying sampling regions of only $0 \leq r \leq 10$ mm and $0 \leq r \leq 7.5$ mm, respectively, the algorithm is not concerned with what happens beyond these boundaries, and, therefore, the field is not constrained in any way in those areas. This brings to light the point that one must be careful to specify a large enough area of interest for the least squares algorithm, if one is to be sure of obtaining a satisfactory field in the entire region of practical usage. Clearly, on the one hand, one is interested in keeping the algorithm data to a minimum from the point of view of computation time, but, on the other hand, one must ensure enough data to avoid degradation of the field in other areas that may still be of interest. A suitable global design to balance these objectives has not yet been investigated, and some degree of trial and error is needed at present to arrive at a satisfactory conclusion.

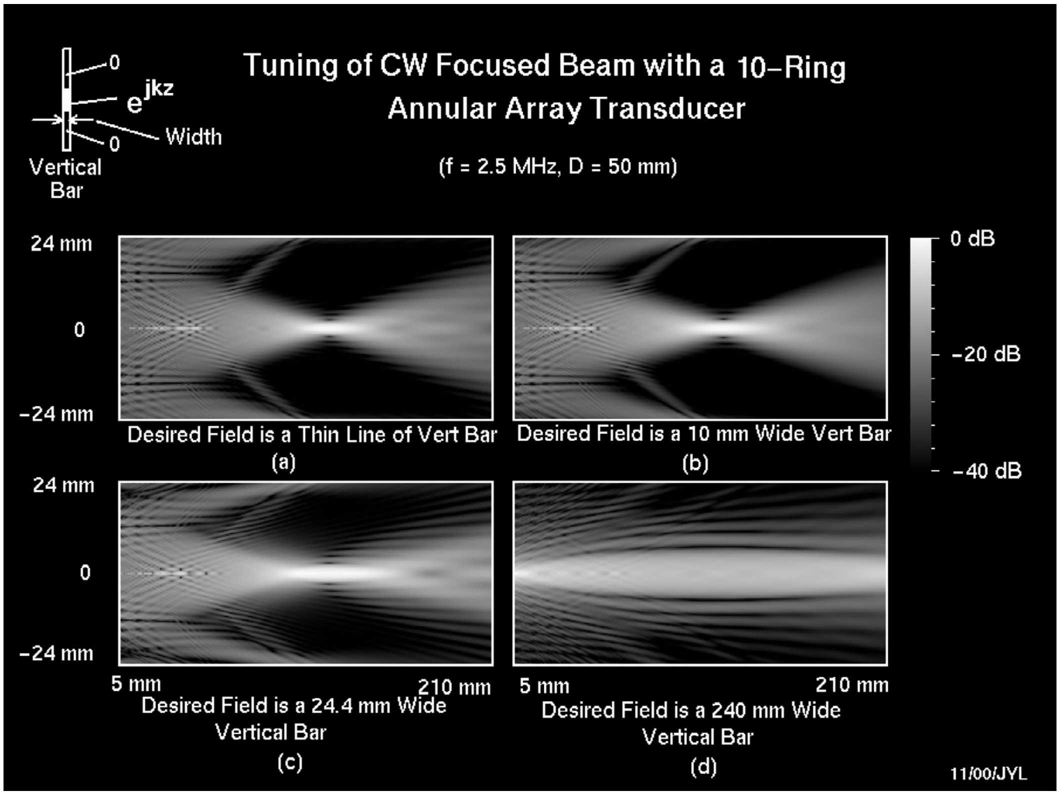


Fig. 11. Tuning results for simple desired fields. a) Tuning using a vertical line through the focus at $z = 120$ mm. The line has a value of zero except in the central portion of a height of 2.54 mm, whose value is $e^{jkz}$ (see upper left-hand corner of the figure). b) Tuning using the same line as in (a) except that the width is 10 mm centered at $z = 120$ mm. c) The same as (a) except that the width is 24.4 mm. d) The same as (a) with width of 240 mm.

### *D. Tuning Using Generalized Field*

Finally, we now also assume that the pre-computed discretized Gaussian field of Fig. 9(a) is not available in practice and consider the more practical problem of tuning based on a simpler design rule. For this, we design a field with a stepwise amplitude distribution based around $r = 0$, $z = 120$ mm, in the form of a vertical bar (with respect to the field plots) as shown in the upper left-hand corner of Fig. 11. The center of the bar is located at the point $r = 0$, $z = 120$ mm defined as the focus of the desired field and the total length (height) of the bar is 48 mm ($0 \leq r \leq 24$ mm) as per the tuning example of Fig. 10(b) previously. The height of the central section $0 \leq r \leq 1.27$ mm with distribution $e^{jkz}$ is 2.54 mm (full-width at half-maximum lateral resolution $GR_L$ in [5]), and the width of bar is changeable while the field outside the range $0 \leq r \leq 1.27$ mm is defined as zero for 1.27 mm $< r \leq 24$ mm. Fig. 11(a) is then the tuning result for a single vertical line sampled at $z = 120$ mm, and Fig. 11(b and c) are for bars of widths 10 mm (b) and 24.4 mm (c) (depth of field $GFz_{\max}$ in [5]). These represent a gradual lengthening of the desired depth of focus between each plot, with this being extended to a total width of 240 mm (double the focal length) in (d). In this latter case, we observe that the extension of the focal zone is achieved at the cost of a significant increase in both the width of the mainlobe and the magnitude of supporting sidelobe levels. See Table IV for quantization amplitudes and phases corresponding to the four panels in Fig. 11. Finally, Fig. 12 shows the convergence of least squares quantization magnitudes $|q_p|$ and phases $\theta_p$ as a function of increasing aperture ratio $a/R$ for the tuning example of Fig. 11(a).

## VIII. Conclusions and Further Work

We have discussed a method for computing and tuning the linear lossless field of flat annular arrays using 1-D Fourier-Bessel series. The series corresponds to a set of Bessel beams propagating into the medium, which, in the limit, provides a linear mapping between the ring pressures on the transducer surface and the field at any point in space. The Fourier-Bessel field calculation method was found to be both quicker and more accurate close to the transducer surface than the Rayleigh-Sommerfeld method with Fresnel approximation when applied to a 10-ring annular array operating at 2.5 MHz in water. The tuning method allowed us to tune the field in different manners by defining different desired fields. However, some degree of trial and error was found to be necessary when employing different design criteria, and this is an area that could benefit from further investigation. It may also be that optimization schemes other than least squares could provide

TABLE IV

Quantization Amplitudes and Phases for Panels in Fig. 11.

| | Ring Number | | | | | | | | | |
|---|---|---|---|---|---|---|---|---|---|---|
| | $p=1$ | $p=2$ | $p=3$ | $p=4$ | $p=5$ | $p=6$ | $p=7$ | $p=8$ | $p=9$ | $p=10$ |
| $\|q_p\| / \|q_1\|$ Fig. 11(a) | 1.000 | 0.984 | 0.982 | 0.979 | 0.990 | 1.017 | 1.034 | 0.993 | 0.861 | 0.682 |
| $\theta_p/\pi$ Fig. 11(a) | 0.488 | 0.341 | 0.012 | −0.506 | 0.789 | −0.109 | 0.797 | −0.490 | 0.052 | 0.479 |
| $\|q_p\| / \|q_1\|$ Fig. 11(b) | 1.000 | 0.986 | 0.989 | 0.993 | 1.001 | 0.995 | 0.937 | 0.787 | 0.539 | 0.225 |
| $\theta_p/\pi$ Fig. 11(b) | 0.485 | 0.343 | 0.012 | −0.508 | 0.781 | −0.126 | 0.774 | −0.509 | 0.053 | 0.521 |
| $\|q_p\| / \|q_1\|$ Fig. 11.(c) | 1.000 | 1.005 | 1.018 | 1.025 | 0.998 | 0.882 | 0.636 | 0.275 | 0.127 | 0.503 |
| $\theta_p/\pi$ Fig. 11(c) | 0.487 | 0.346 | 0.012 | −0.517 | 0.757 | −0.167 | 0.720 | −0.553 | 0.845 | −0.612 |
| $\|q_p\| / \|q_1\|$ Fig. 11(d) | 1.000 | 0.355 | 0.191 | 0.127 | 0.092 | 0.072 | 0.058 | 0.050 | 0.040 | 0.048 |
| $\theta_p/\pi$ Fig. 11(d) | 0.290 | 0.174 | −0.035 | −0.319 | −0.682 | 0.868 | 0.329 | −0.230 | 0.972 | 0.320 |

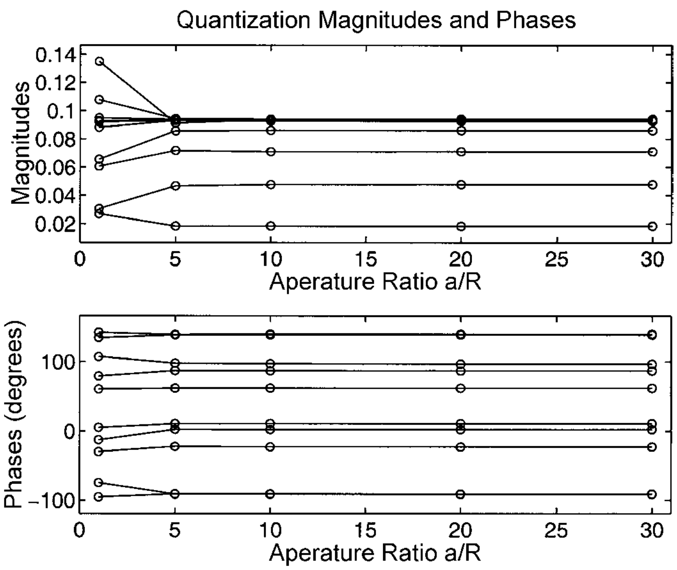


Fig. 12. Convergence of quantization magnitudes $|q_p|$ and phases $\theta_p$ as a function of aperture ratio $a/R$ for tuning example in Fig. 11(b).

benefits. There remain also several other extensions to the current method that require investigation. First, extension of the analysis to pulse wave (PW) fields both for field computation and tuning. Second, the current analysis is limited to annular arrays and its development of non-annular arrays both in CW and PW cases is of interest for more widespread application. This will require the use of 2-D Fourier-Bessel series, which are capable of modelling quantization profiles and fields that are non-circular-symmetric around the propagation axis. Some initial work has already begun on this, but there are many computational aspects still to be investigated; these are partly due to the increased number of transducer elements in such arrays and partly due to the fact that 2-D Fourier-Bessel series require the computation of 2-D Fourier-Bessel coefficients. In principle, the analysis for both field computation and tuning of 2-D series follow the same general structure as in the 1-D case. However, it may be that the increased numerical complexity of such schemes provide difficulty in implementation because of computational time, memory, or numerical stability requirements. An extension of all of these methods to a suitable model for lossy media is also of interest.

## Acknowledgment

The authors thank the anonymous reviewers for their helpful comments in improving the presentation of the paper.

## References


[1] G. Tolstov, *Fourier Series.* New York: Dover Publications Inc., 1962.

[2] F. Bowman, *Introduction to Bessel Functions.* New York: Dover Publications Inc., 1958, pp. 15–17.

[3] J. A. Stratton, *Electromagnetic Theory.* New York: McGraw-Hill Book Company, 1941, p. 356.

[4] J. Durnin, “Exact solutions for nondiffracting beams. I. The scalar theory,” *J. Opt. Soc. Amer.*, vol. 4, no. 4, pp. 651–654, Apr. 1987.

[5] J.-Y. Lu and J. F. Greenleaf, “Ultrasonic nondiffracting transducer for medical imaging,” *IEEE Trans. Ultrason., Ferroelect., Freq. Contr.*, vol. 37, no. 5, pp. 438–447, Sep. 1990.

[6] ——, “Sidelobe reduction for limited diffraction pulse-echo systems,” *IEEE Trans. Ultrason., Ferroelect., Freq. Contr.*, vol. 40, no. 6, pp. 735–746, Nov. 1993.

[7] ——, “Nondiffracting X waves—Exact solutions to free-space scalar wave equation and their finite aperture realizations,” *IEEE Trans. Ultrason., Ferroelect., Freq. Contr.*, vol. 39, no. 1, pp. 19–31, Jan. 1992.

[8] S. Holm, “Bessel and conical beams and approximation with annular arrays,” *IEEE Trans. Ultrason., Ferroelect., Freq. Contr.*, vol. 45, no. 3, pp. 712–718, May 1998.

[9] P. D. Fox and S. Holm, “Decomposition of acoustic fields in quantized Bessel beams,” in *Ultrason. Proc. WCU’99/UI’99*, vol. 38, pp. 190–194.

[10] C. Lee and P. J. Benkeser, “Computationally efficient sound field calculations for a circular array transducer,” *IEEE Trans. Ultrason., Ferroelect., Freq. Contr.*, vol. 39, no. 1, pp. 43–47, Jan. 1992.

[11] L. X. Yao, J. A. Zagzebski, and E. J. Boote, “Fast algorithm to calculate ultrasound pressure fields from single-element transducers,” *IEEE Trans. Ultrason., Ferroelect., Freq. Contr.*, vol. 36, no. 4, pp. 446–451, 1989.

[12] P. R. Stepanishen, “Acoustic transients from planar axisymmetric vibrators using the impulse response approach,” *J. Acoust. Soc. Amer.*, vol. 70, no. 1176, pp. 1176–1181, 1981.

[13] D. P. Orofino and P. C. Pedersen, “Efficient angular spectrum decomposition of acoustic sources-part i: Theory,” *IEEE Trans. Ultrason., Ferroelect., Freq. Contr.*, vol. 40, no. 3, pp. 238–249, May 1993.

[14] ——, "Efficient angular spectrum decomposition of acoustic sources-part ii: Results," *IEEE Trans. Ultrason., Ferroelect., Freq. Contr.*, vol. 40, no. 3, pp. 250–257, May 1993.

[15] P. D. Fox and S. Holm, *Tuning of Bessel Beams on Annular Arrays*. vol. 25, ser. Acoustical Imaging, Halliwell and Wells, Eds. New York: Kluwer Academic/Plenum Publishers, 2000, pp. 51–57.

[16] ——, "Modeling of CW annular arrays using limited diffraction Bessel beams," *IEEE Trans. Ultrason., Ferroelect., Freq. Contr.*, vol. 49, no. 1, pp. 85–93, Jan. 2002.

[17] J.-Y. Lu, "Designing limited diffraction beams," *IEEE Trans. Ultrason., Ferroelect., Freq. Contr.*, vol. 44, no. 1, pp. 181–193, Jan. 1997.

**Paul Fox** was born in Sheffield, England to an English father and French mother. In 1987 he completed a B.A. Hons Engineering Science degree at the University of Oxford, England. During in 1988 he was Research Assistant at the Department of Aeronautical Engineering, University of Sydney, Australia, and later became Research Assistant at the Department of Cybernetics, University of Reading, England from 1988–1991. From 1991–1995 he remained there to complete a part time Ph.D. in mathematical modeling and signal processing, before becoming Research Fellow in control theory and system identification at the University of Warwick, England from 1995–1998. He then moved to Norway from 1998–2000 as a European Union Marie Curie Research Fellow to work with Professor Sverre Holm on limited diffraction beams at the ultrasound at the Department of Informatics, University of Oslo. Following this he spent the last four months of 2000 as Postdoctoral Research Fellow in limited diffraction beams with Professor Jian-yu Lu at the Ultrasound Laboratory, Department of Bioegineering, University of Toledo, Ohio, USA. More recently he has been a postdoctoral researcher in ultrasound at the Sensors Lab, Department of Engineering Science, University of Oxford, UK from July 2001 to April 2002. As of May 2002 he became postdoctoral researcher in medical ultrasound at Orsted. DTU, Technical University of Denmark. His current main interests are in field propagation and beamforming with emphasis in medical applications.

**Jiqi Cheng** was born in Jiangsu, China, in 1975. He received the B.S. degree and the M.S. degree in biomedical engineering in 1998 and 2000 respectively, both from Southeast University, Nanjing, China. He is currently pursing his doctorate degree in the Department of Bioengineering at the University of Toledo, OH.

His research interests in ultrasound include field calculation, beam forming, transducer modeling, and medical imaging.

**Jian-yu Lu** (S'86–M'88–SM'99) is currently a professor in the Department of Bioengineering at the University of Toledo, Toledo, OH, and an adjunct professor of medicine at the Medical College of Ohio, Toledo, OH. He has been the Graduate Director of the Department of Bioengineering at the University of Toledo since 1999. Before joining the University of Toledo as a professor in September 1997, he was an associate professor of biophysics at the Mayo Medical School and an associate consultant at the Department of Physiology and Biophysics, Mayo Clinic/Foundation, Rochester, MN. His research interests are in acoustic imaging and tissue identification, medical ultrasonic transducers, and ultrasonic beam forming and propagation.

Dr. Lu has published many papers in peer-reviewed journals. Two of his papers published in the IEEE Transactions on the Ultrasonics, Ferroelectrics, and Frequency Control (UFFC) in 1992 have received the Outstanding Paper Award from the UFFC society for the discovery of X waves that, in theory, can propagate to an infinite distance without spreading (diffraction-free). These waves have potential applications in medical imaging (in both ultrasound and optics).

Dr. Lu has received the Edward C. Kendall (a Nobel Laureate at Mayo Clinic) Award from the Mayo Alumni Association, Mayo Foundation, in 1992, for his meritorious research; the FIRST Award from the National Institutes of Health (NIH) in 1991; and the Biomedical Engineering Research Grant Award from the Whitaker Foundation in 1991, in addition to other long-term R01 type of NIH grant award.

Dr. Lu is the Editor-in-Chief of the *IEEE Transactions on Ultrasonics, Ferroelectrics, and Frequency Control*. He was the Technical Program Chair of the 2001 IEEE International Ultrasonics Symposium—a joint meeting with the World Congress on Ultrasonics held in Atlanta, GA, in October 2001. He has been an Exhibition Chair of the IEEE Ultrasonics Symposia for many years and is a member of the Technical Program Committee of Group I (Medical Ultrasonics). He serves in both the UFFC Web Committee and the UFFC Ultrasonics Committee. Dr. Lu is a senior member of the IEEE UFFC Society and a senior member of the American Institute of Ultrasound in Medicine (AIUM). He is also a managing editor of the online journal Frontiers in Bioscience.